New Journal of Physics
The open access journal at the forefront of physics

Deutsche Physikalische Gesellschaft DPG IOP Institute of Physics

PAPER • OPEN ACCESS

Multidimensional photoemission spectroscopy—the space-charge limit

To cite this article: B Schönhense *et al* 2018 *New J. Phys.* **20** 033004

New Journal of Physics
The open access journal at the forefront of physics

Deutsche Physikalische Gesellschaft DPG
IOP Institute of Physics

Published in partnership with: Deutsche Physikalische Gesellschaft and the Institute of Physics

OPEN ACCESS

RECEIVED
9 September 2017

REVISED
29 November 2017

ACCEPTED FOR PUBLICATION
18 December 2017

PUBLISHED
5 March 2018

PAPER

Multidimensional photoemission spectroscopy—the space-charge limit

B Schönhense[1], K Medjanik[2], O Fedchenko[2], S Chernov[2], M Ellguth[2], D Vasilyev[2], A Oelsner[3], J Viefhaus[4], D Kutnyakhov[4], W Wurth[4,5], H J Elmers[2] and G Schönhense[2]

[1] Department of Bioengineering, Imperial College, London, United Kingdom
[2] Institut für Physik, Johannes Gutenberg-Universität Mainz, Germany
[3] Surface Concept GmbH, Mainz, Germany
[4] DESY Hamburg, Germany
[5] Physics Department and CFEL, Universität Hamburg, Germany

E-mail: b.schoenhense14@imperial.ac.uk

Keywords: space-charge effect, photoemission spectroscopy, time-resolved photoemission

Supplementary material for this article is available online

Abstract

Photoelectron spectroscopy, especially at pulsed sources, is ultimately limited by the Coulomb interaction in the electron cloud, changing energy and angular distribution of the photoelectrons. A detailed understanding of this phenomenon is crucial for future pump–probe photoemission studies at (x-ray) free electron lasers and high-harmonic photon sources. Measurements have been performed for Ir(111) at $h\nu = 1000$ eV with photon flux densities between $\sim 10^2$ and 10^4 photons per pulse and μm^2 (beamline P04/PETRA III, DESY Hamburg), revealing space-charge induced energy shifts of up to 10 eV. In order to correct the essential part of the energy shift and restore the electron distributions close to the Fermi energy, we developed a semi-analytical theory for the space-charge effect in cathode-lens instruments (momentum microscopes, photoemission electron microscopes). The theory predicts a Lorentzian profile of energy isosurfaces and allows us to quantify the charge cloud from measured energy profiles. The correction is essential for the determination of the Fermi surface, as we demonstrate by means of '*k*-space movies' for the prototypical high-Z material tungsten. In an energy interval of about 1 eV below the Fermi edge, the bandstructure can be restored up to substantial shifts of ~7 eV. Scattered photoelectrons strongly enhance the inelastic background in the region several eV below E_F, proving that the majority of scattering events involves a slow electron. The correction yields a gain of two orders of magnitude in usable intensity compared with the uncorrected case (assuming a tolerable shift of 250 meV). The results are particularly important for future experiments at SASE-type free electron lasers, since the correction also works for strongly fluctuating (but known) pulse intensities.

1. Introduction

The field of photoelectron spectroscopy and microscopy has seen decades of continuous improvement of analysers and excitation sources. The energy resolution has been driven to amazing limits ranging from sub-meV at low energies to the 10 meV region in the soft x-ray regime [1]. High angular resolution (down to $<0.1°$) or spectroscopy up to the hard x-ray range demand small footprints of the photon beam on the sample surface. The vast majority of today's high-performance photon sources are pulsed, with lengths down to the fs range for lasers, sources based on high-harmonic generation (HHG) or free-electron lasers (FELs). The high density of electrons released by intense, short photon pulses in a small area on the sample leads to significant Coulomb interaction, which alters the energy and angular distribution and sets the ultimate limit to the performance of photoemission experiments. Depending on the number of electrons in the cloud and their spatio-temporal distribution, this effect can deteriorate the photoelectron spectra dramatically [1–11].

Although the conditions (pulse intensity, pulse length and repetition rate) are quite different for synchrotron radiation sources, FELs or HHG sources, the Coulomb forces manifest comparably. Footprints of the photon beam with sizes on the order of 10 μm diameter are becoming standard at modern high-brilliance beamlines; photon pulse lengths range from ~70 ps for storage ring sources down to <100 fs for FEL and HHG sources. In such a small initial confinement (in space and time) the high electron density gives rise to large Coulomb forces and *e*–*e* scattering processes. When the cloud is expanding, the scattering rate drops but the integral long-range Coulomb forces persist up to macroscopic distances. In the cases discussed below there is still significant interaction up to 80 mm from the sample surface.

It has long been known that the Coulomb interaction of an individual electron with all other electrons leads to energy shifts and changes of electron trajectories, in electron microscopy termed the Boersch effect [12, 13]. Fully considering the many-body system, an electron feels a Coulomb term from each other electron. Then we can approximate the cloud of electrons as a space-charge continuum with some density, and we take the 'average' of that as the origin of the effective force. This 'deterministic' component has been considered in much detail and was even discussed as a means for aberration correction [14]. In addition, individual *e*–*e* scattering events occur stochastically, causing irreversible changes in energy and momentum (thermal broadening). These make up the stochastic component of the Coulomb term. Note that the stochastic and deterministic terms are decoupled. The deterministic contribution can be seen as an approximation based on a homogenised charge-density distribution (or a deterministic source of equidistantly spaced electrons). The stochastic component is a result of inhomogeneities in the charge distribution and reflects the stochastic nature (granularity) of the photoelectron beam. The usual strategy to cope with the space-charge problems is to reduce the charge per pulse.

In photoemission, the major contribution to space-charge induced energy shifts stems from the large number of secondary electrons. Intense clouds of slow electrons can also occur in pump-and-probe experiments when the pump laser gives rise to multiphoton photoemission [5–10]. The coexistence of a small number of fast photoelectrons with a large number of slow electrons (from the secondary cascade or generated by a pump laser) leads to a specific behaviour due to the different longitudinal and transversal momentum components of the two species. The slowly travelling charge cloud exerts an anisotropic force on the rapidly expanding photoelectron distribution.

The space-charge effect becomes particularly severe in the x-ray range, see e.g. [3]. The cascade of inelastic scattering events of photoelectrons as a 'multiplication effect' has maximum effectiveness in soft x-ray photoemission. At $h\nu = 1000$ eV our measurements for the Ir(111) surface reveal a total electron yield of ~0.1 *e*/photon. Assuming a photon flux of $\sim 10^7$ photons per pulse (a typical value for the experiments shown below), each photoelectron from the valence-band is accompanied by a cloud of secondary electrons of the order of 0.1 1 pC.

We present a combined experimental, analytical and simulated study of the space-charge effect in multidimensional photoemission (resolving all three momentum coordinates and the energy in the present experiment) using cathode-lens type instruments. The electrostatic field between sample surface and anode and the subsequent immersion lens optics cause a special signature of the space-charge effect. The cloud of slow electrons travels close to the optical axis along the surface normal, whereas the fast photoelectrons form a rapidly expanding disc due to their larger transversal momentum. Based on a hybrid approach of analytical treatment and ray-tracing calculations, we propose a model that predicts a Lorentzian shape of the energy isosurfaces, in good agreement with experiment. A fit of the general functional expression to the measured shape of the isosurfaces disentangles the isotropic acceleration in the homogeneous electrostatic field and the anisotropic acceleration in the lens field. Exploiting the different signature of the space-charge effect in these two regimes, the fit yields the value for the total charge of the low-energy electrons. An algorithm is presented that can correct the deterministic part of the Coulomb interaction. The correction yields intact momentum distributions at space-charge induced energy shifts up to ~7 eV, corresponding to an intensity gain of 2 orders of magnitude in comparison to similar measurements without correction. The stochastic contribution from individual scattering events appears as an increased diffuse background intensity in the spectral region some eV below the Fermi edge. The region close to the Fermi energy is least affected by this blur since the electrons 'surviving' at this energy did not suffer inelastic scattering events. The correction is crucial for the determination of Fermi surfaces as we demonstrate by the example of the prototypical high-Z material tungsten. '*k*-space movies' reveal that uncorrected distributions lead to missing features in the Fermi surface.

More generally, the present study yielded a better understanding of space-charge effects in strong electric fields. Since the correction is based on an analytical expression, it can be applied even in cases of strong (but quantitatively known) fluctuations of the pulse intensities. Such conditions are found at SASE-type free electron lasers where the intensity of each individual photon pulse can be monitored and used for the correction of the corresponding individual electron events. It can be expected that the correction algorithm described in this paper will be most important for future photoemission experiments at FELs using the momentum microscopy

technique. Since the delay between 'pump' (intense fs laser pulse) and 'probe' (FEL or HHG pulse) can be modelled using the same algorithm, extended (complete) correction schemes for ultrafast time-resolved photoemission experiments are possible.

2. Experimental results

2.1. Multidimensional photoemission spectroscopy

The discovery of exciting electronic systems such as topological insulators, topological semimetals, Weyl systems or novel superconducting materials has posed a challenge for angular-resolved photoemission experiments. The focus has shifted to complex questions regarding topologies in k-space, the number of Fermi-level crossings of bands, or the spin texture, which is a fingerprint for time-reversal invariance. The quantities which contain the complete information on the electronic structure are the *spectral density function* $\rho\,(E_B, \boldsymbol{k})$ and the corresponding *spin-polarisation vector* $\boldsymbol{P}\,(E_B, \boldsymbol{k})$. The measured quantity $I\,(E_B, \boldsymbol{k})$ is the discretized experimental representation of ρ, weighted by the transition matrix element. In the general case of a bulk sample, the 4D data array I contains the information on all band dispersions, partial and total band gaps, the Fermi surface and all other energy isosurfaces, and the effective mass. $\boldsymbol{P}$ describes the spin texture which often (e.g. for most topological surface states) is composed of three independent vector components. Hence, for a bulk electronic system with spin texture the full information is contained in a scalar and a vector function in 4D parameter space: $[I, \boldsymbol{P}]\,(E_B, \boldsymbol{k})$.

The experimental approach of recording these quantities can be termed *multidimensional photoemission spectroscopy*. Four classes of instruments have been developed in order to tackle this problem: Hemispherical analysers can detect a certain angular range along one direction (up to $+/-15°$ with good angular resolution) and an energy interval (up to several eV) in parallel. The perpendicular angular direction can be accessed either via sample rotation or using a deflector arrangement and sequential recording [15, 16]. The angular coordinates have to be converted into momentum coordinates. These analysers have reached a high degree of maturity with energy resolution down to <1 meV and angular resolution $<0.1°$. The identical lens systems have recently been combined with time-of-flight (ToF) energy recording, constituting a new family of angular-resolving ToF spectrometers [17, 18]. The most recent approaches employ a cathode lens to visualise directly the 'k-image', i.e. the pattern of the transversal momentum components. The required energy resolution can be implemented either in terms of a dispersive analyser [19] or via ToF recording [20]. The dispersive-analyser approach is independent of the time structure of the photon source which, for continuous sources, bears the advantage of the minimum space-charge effect. The ToF-approach requires pulsed photon sources such as lasers, HHG sources, storage rings or FELs; its advantage is parallel energy recording. Simultaneous detection of a (k_x, k_y) momentum range exceeding the first Brillouin zone and an energy range of E_{kin} comprising the d-band complex of a transition metal yields maximum degree of parallelisation. Hence the ToF-method is ideal for developing a correction algorithm of the space-charge effect and has thus been used for the present experiments.

Combined with an imaging spin filter, the ToF-approach allows us to measure data arrays of one spin component $P\,(E_B, k_x, k_y)$; in the future even all three components [21]. Existing imaging spin filters are not yet fully optimised; however first results look very promising [22, 23]. Due to the rather narrow spin-asymmetry profiles, the results of the present study have essential consequences for spin-filtered k-imaging in the presence of significant space-charge shifts.

2.2. Space-charge effect in k-microscopy using soft x-rays

Momentum microscopes are based on a special type of cathode lens (objective lens with a strong immersion field in front of the sample), being optimised for full-field imaging of a large momentum range (k_x, k_y) at high k-resolution [19, 20]. The photoelectron distribution is detected directly in k-space by imaging of the Fourier plane which represents a cross section through the k-sphere with radius defined by the final-state energy. Here we used ToF parallel energy recording, but all considerations and evaluations apply equally to k-microscopes with dispersive energy analysers, and also to photoemission electron microscopes (PEEMs).

We have investigated the space-charge induced effects at $h\nu = 1000$ eV using the high-brilliance photon beam of beamline P04 at PETRA III (DESY, Hamburg). In a k-space microscope the k-image is formed in the backfocal plane of the cathode lens (for details, see e.g. [19]). A subsequent lens system projects this image of the transversal momentum components onto the time-resolving image detector (delay-line detector [24, 25]), with variable magnification. The kinetic energy E_{kin} is recorded in an interval of several eV width via the ToF. This novel technique is capable of recording the 4D spectral density function $\rho\,(E_B, \boldsymbol{k})$ in the entire Brillouin zone and d-band complex within a few hours (for details, see [20]).

In order to study the signature of the increasing Coulomb interaction, we varied the photon flux by gradually opening the exit slit of the monochromator. Slit widths of 10, 100, 300, 1000 and 1500 μm yielded values of

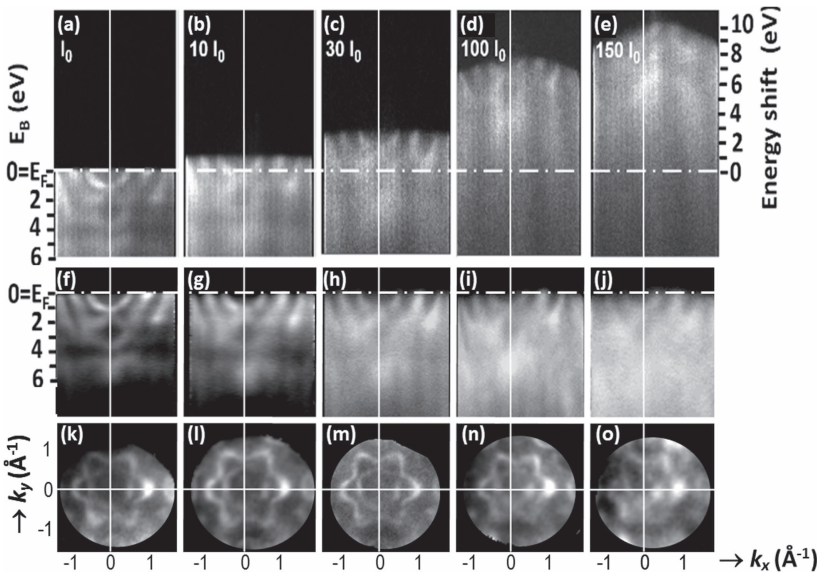

Figure 1. Space-charge induced deformation of the spectral distribution $I(E_{kin}, k_x, k_y)$ for the Ir(111)-surface at hν = 1000 eV. In order to probe a large $k_{||}$-range, the image has been adjusted to the Fermi-surface cut in the first repeated Brillouin zone along k_y. (a)–(d) show electron distributions at four kinetic energies as given in the panels, taken at a photon intensity of 100 I_0. (e), (f) E_{kin}-*vs*-k_y and -k_x sections for a photon intensity of 150 I_0, revealing a space-charge induced acceleration of up to 10 eV at $k_{||} = 0$. The dashed curve in (e) denotes the fit, the dash-dotted line denotes the position of the Fermi energy in case of absence of space-charge interaction.

$\sim 10^{12}$ to 10^{14} photons per second at 5 MHz pulse rate [26] in a photon footprint of about 35 μm on the sample surface. In the following these settings are referred to as I_0, 10 I_0, 30 I_0, 100 I_0 and 150 I_0, respectively.

The momentum dependence of the space-charge interaction has been visualised in a large radial range by adjusting the field of view off-centre, reaching a maximum radius of almost 4 Å^{-1}. Figure 1 shows sections through as measured data arrays $I(E_{kin}, k_x, k_y)$ for an Ir(111) sample. The constant-energy sections (first row) were taken for the intensity level of 100 I_0. Given the photon energy of 1000 eV and a work function of ~5 eV the maximum kinetic energy (at the Fermi level) is expected at ~995 eV. Instead, we observe the onset of the electron distributions at kinetic energies of 1002 eV for an intensity of 100 I_0 (figure 1(a)) and 1005 eV for 150 I_0 (e, f). It means that the respective space-charge induced energy gains for 100 I_0 and 150 I_0 are 7 eV and 10 eV, respectively.

The kinetic energy sequence in the top row of figure 1 reveals how the distribution starts on the optical axis, here at the bottom corner of image (a) and then gradually moves upwards (b–d). In (d) the cutoff has reached the top corner. For the E_{kin}-*vs*-$k_{||}$ sections measured at 150 I_0 (e, f) the space-charge induced shift reaches its maximum of 10 eV on the axis and drops to half of this value at 3.5 Å^{-1}, see (e). The cut along the radial direction, here E_{kin}-*vs*-k_y, reveals the profile shown in panel (e), which can be readily fitted by a Lorentzian curve (see theory section). The E_{kin}-*vs*-k_x cut (f) intersects the Lorentzian profile in a transversal direction. The correct position of the Fermi edge for vanishing space-charge interaction is denoted by the dash-dotted line in (e, f). This position is determined by reducing the photon flux to I_0 as discussed in the next section (cf. figure 2(a)). Despite the strong energy shift and distorted E_{kin}-*vs*-$k_{||}$ cuts, the section close to E_F (panel d) is surprisingly well preserved, even in these raw data. The deformation of the energy isosurfaces is caused by the net Coulomb force exerted on the photoelectrons by the large amount of slow electrons travelling close to the optical axis in the acceleration field above the sample surface and in the lens field of the cathode lens.

2.3. Correction of the space-charge effect

Figure 2 shows a systematic study of the changes of the spectral distribution functions for five different values of the photon flux, revealing details of the signature of Coulomb interaction in the beam. Columns 1–5 display the results for intensities I_0 to 150 I_0, corresponding to photon flux densities between $\sim 10^2$ and $\sim 10^4$ photons per pulse and μm^2. The first row shows the energy shift and deformation of the Fermi cutoff. Starting from the lowest flux I_0 (10 μm exit slit) the intensity was increased by a factor of 10, 30, 100 and 150. The corresponding space-charge induced shifts of the kinetic energy reach maxima of 0.8, 2.8, 7.4 and 10 eV, respectively. For (e) the total electron count rate in the delay-line detector, corresponding to the topmost 20 eV of the photoelectron spectrum and the given k-region, was $\sim 5 \times 10^6$ cps.

The functional form of the Lorentzian (given in equation (5) in section 3.3) was fitted to the shape of the Fermi-level cutoff taken from the as-measured (t_F, k_x, k_y) raw data stacks; t_F is the ToF corresponding to this

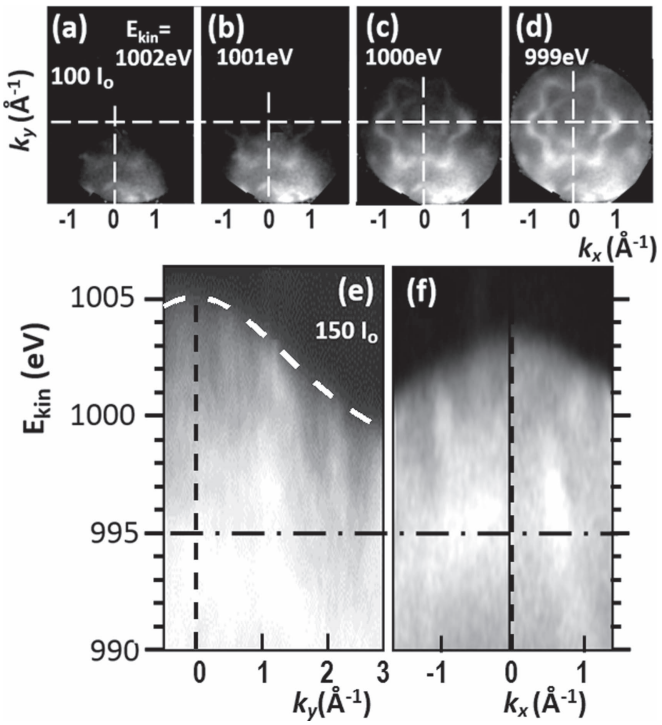

Figure 2. Sequence of distributions for Ir(111) taken at identical settings but different photon intensities (I_0 to 150 I_0) between ~10^5 (column 1) and ~10^7 (column 5) photons per pulse. E_B-*vs*-k_x cuts through the as-measured data (a-e) are compared with corresponding cuts after space-charge correction (f)–(j). In the corrected sections the deterministic part of the Coulomb interaction is eliminated by fitting a generic functional expression to the Fermi-level cutoffs in the stacks corresponding to (a)–(e) and re-normalising the energy scale. What remains is the stochastic contribution, visible in the enhanced diffuse background of inelastically-scattered electrons (increasing in sequence (f)–(j)). At the Fermi cutoff the band contours resulting from a section through the 3D Fermi surface persist up to intensity 100 I_0 (k)–(n). At 150 I_0 (o) they are still visible but appear strongly blurred.

cutoff. For strongly structured momentum patterns at the Fermi energy, an array of points used for interpolation has proven superior to a fully automatised procedure because it better accounts for low-intensity regions. Next, the data stack is corrected according to the parameter set obtained by the fit. The corrected sections are shown in the second row of figure 2. The deformation has disappeared, the Fermi cutoff is straight and coincides for all distributions (dash-dotted lines in (f–j)).

The contribution of the stochastic *e–e* scattering events is clearly visible in terms of the increasing diffuse background intensity that sets in at 30 I_0 and becomes very significant at higher intensities. In the sequence (f, g, h, i, j) the brightness in the lower part of the panels increases dramatically and finally masks the band features. We see, however, that the background intensity is smaller near the Fermi cutoff. This gives a hint on the nature of the individual *e–e* scattering processes. These processes are most likely to occur close to the sample surface, where the electron density is high and the velocity-dependent separation of the electrons did not yet set in. Photoelectrons from the valence range preferably scatter at low-energy cascade electrons because of their large number. When scattering with a slow electron, the fast electron loses energy and momentum. The electrons that escape from the cloud with initial energies close to the Fermi cutoff did not suffer from such scattering events and hence largely retained their initial distribution.

Despite the space-charge induced energy shift, the band features are quite well conserved within an interval of approx. 1 eV from E_F. The 30 I_0 pattern shows almost no deterioration in the region close to E_F. Section (m) appears even slightly better focused than (k) and (l); most likely the space-charge shift of 3 eV at 30 I_0 compensates a slight defocusing at I_0 and 10 I_0. At 100 I_0 an additional blur of the bands is evident (i, n) and finally at 150 I_0 this blur, together with the diffuse background, masks the band features (j, o). In panels (n, o) the band pattern shows a significant reduction in size. Upon scattering with a slow electron, the fast photoelectron also loses momentum. In this regime of very high scattering probability longitudinal momentum might also be lost, resulting in a (stochastic) contribution to the total energy shift, counteracting the deterministic shift.

Part of the blur in figure 2(h)–(j) originates from the increasing photon bandwidth of 35, 170 and 500 meV for I_0, 10 I_0 and $\geq$30 I_0, respectively. Above 30 I_0 the field-of-view acts like a virtual exit slit. We conclude that two orders of magnitude in usable intensity is gained by the correction, if the interest is focused on the bands close to E_F.

3. Theoretical model

3.1. Ray-tracing simulations for cathode lenses

Prior to the development of the analytical model, we performed simple ray-tracing simulations [27] (without space-charge and for the short-pulse limit) for five initial kinetic energies: 1 eV representing the secondary cascade electrons (which in reality extend over several eV), 16 eV being a typical photoelectron kinetic energy in the VUV (e.g. for table-top HHG sources), 120 eV is typical for EUV excitation at Synchrotron-radiation sources, 1 keV represents a soft x-ray energy and 3.5 keV corresponds to the tender (or lower end of the hard) x-ray regime. The simulation assumed a source spot on the sample surface of 35 μm, identical to our experimental conditions.

Figure 3 shows the spatio-temporal behaviour of the 1 eV electrons (black rays) together with the four species of faster electrons. Panels (a–c) show the results for 16 eV, 120 eV and 1 keV in the first 30 mm from the sample surface. These data were simulated for the standard lens geometry with 4 mm gap, used in the experiments. The result for 3.5 keV (panel d) corresponds to a larger region of about 60 mm, simulated for a new high-energy lens with 10 mm gap, developed for soft, tender and hard x-ray excitation. This lens accepts an order of magnitude larger *k*-space area than the standard lens.

The ray patterns can be separated into three regimes with different signatures of the Coulomb interaction. In the initial stage close to the surface (*stochastic regime A*) all electrons are confined in the region-of-interest (ROI), which here is 35 μm diameter. Fast and slow electrons are not yet separated, the electron density is high, and individual *e–e* scattering events happen. The origin of the stochastic events lie in the fact that the electron beam itself originates from a stochastic process; the Coulomb interaction between all electrons is of course fully deterministic. Since the slow electrons outnumber the fast ones by several orders of magnitude, the latter experience predominantly inelastic scattering events with loss of energy and momentum. Hence, *scattered electrons show up as diffuse background in the region several eV below* E_F. In this early stage, there is only a small net acceleration due to compensation of Coulomb forces in all directions. An inhomogeneous footprint of the photon beam can induce a net radial force in this initial phase. This can be important in pump-and-probe experiments if the two beams are not exactly concentric or if the pump beam causes inhomogeneous emission patterns. Then the early phase can be characterised by strong inhomogeneous forces acting in various directions, depending on the emission pattern.

The experimental data in section 2 do not show effects of a radial force on the momentum patterns, so we conclude that the influence of the photon beam profile is negligible under our experimental conditions. Instead, the momentum patterns appear broadened at very high photon intensities, revealing that in region *A* elastic scattering events between two fast electrons can also occur. In the vicinity of the surface, the image charge induced in a metallic sample surface causes an attractive force towards the surface [28]. In non-metallic systems, long-lived photoholes in the material cause a similar effect [29].

In the acceleration field between sample surface and anode (*radially uniform force regime B*) the electron cloud of a given energy expands isotropically in an accelerated inertial system (acceleration $a = -e\varepsilon/m$; for electric field strength ε). The electrons stay on hemispherical shells that expand linearly with their initial velocities; the snapshots at 50, 100 and 150 ps in figure 3(a), (b) capture this situation. For 1 eV, 16 eV and 120 eV the distributions represent the full half space above the sample. For 1 and 3.5 keV the objective lens cannot image the full half space, so we restricted the simulated angular range to $+/-18^\circ$ (corresponding to momentum discs with diameters of 10 and 18 Å^{-1}). Due to their larger momenta, the shells of the photoelectrons expand more rapidly than the cloud of the slow secondary electrons. The initial photoelectron momenta are 2, 5.5, 16 and 30 Å^{-1} for $E_{kin} = 16$, 120, 1000 and 3500 eV, respectively. In comparison, the momentum of the 1 eV electrons is only 0.5 Å^{-1}. This leads to an isotropic separation between photoelectrons and slow electrons of 0.2, 0.6, 1.8 and 3.4 mm after 100 ps (cf. panels a, b, c and d). In regime *B*, the Coulomb repulsion by the slowly expanding cloud of secondary electrons leads to a *uniform radial acceleration* of the fast photoelectrons, regardless of their direction. For slow laser-induced electrons the situation is different because the different instants of emission of slow and fast electrons lead to a shift in the centres of the expanding shells.

The saddle point of the potential in the anode bore marks the beginning of the *non-uniform force regime C*, where the decelerating forces cause a deformation of the electron shells. The anode bore (in particle optics termed aperture lens [13]) has the unusual property of being diverging, as visible in the ray paths. It forms a virtual source spot in front of the sample at a distance of 1/3 of the gap distance [30]. In the strongly decelerating field behind the aperture lens the electron shells attain an increasingly flattened (oblate) shape as visible most pronounced in the VUV-case (a) above 400 ps and in the tender x-ray case (d) at 300 ps, where the distributions are close to planar discs. Now the cloud of slow electrons exerts a non-uniform force on the photoelectron discs with its maximum at the optical axis where the distance is minimal. Due to the non-isotropic Coulomb repulsion, the energy distribution of the photoelectrons at the Fermi energy approximately attains a Lorentzian shape (see section 3.2). In all cases, the isotropic shift extends from threshold to ~150 ps, whereas the anisotropic

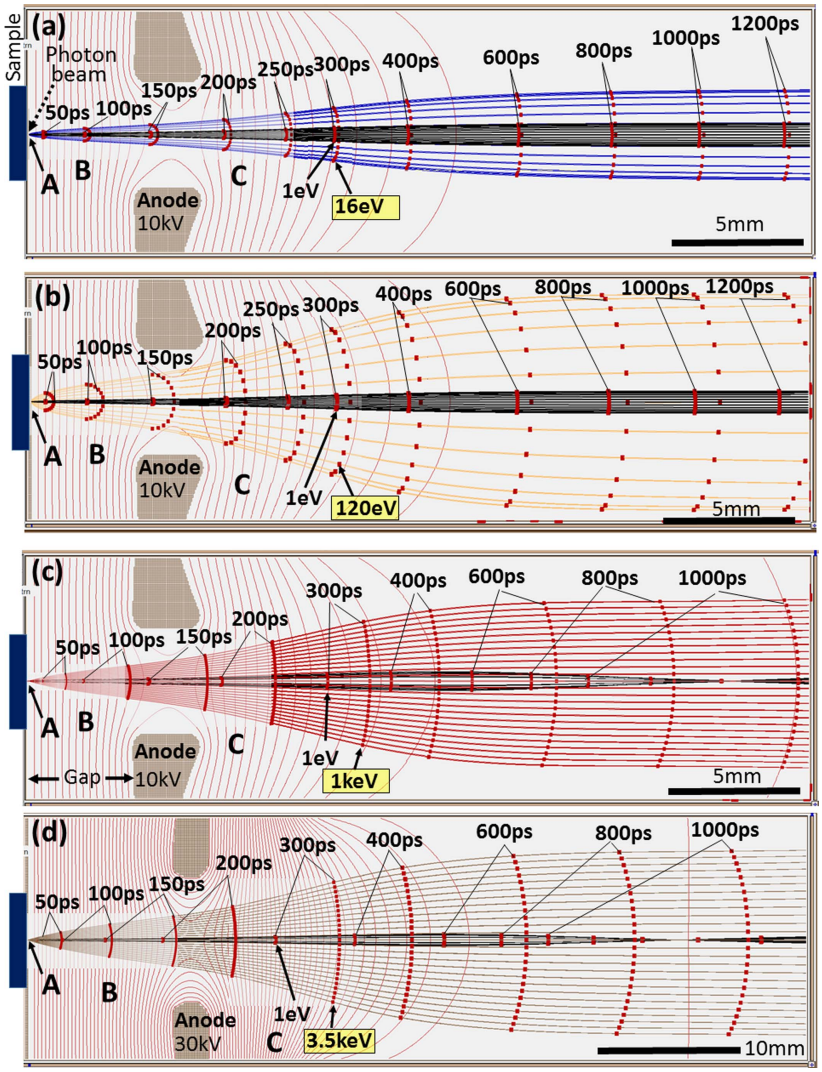

Figure 3. Calculated electron trajectories for photoelectrons representing four spectral regimes: VUV, kinetic energy 16 eV (a); EUV, 120 eV (b); soft , 1 keV (c) and tender x-ray regime, 3.5 keV (d). The black rays show 1 eV electrons, representing the secondary or laser-excited electrons. Thin lines mark equipotential contours, dots denote ToF isochrones with respect to the photon pulse (defining 0 ps). In the *stochastic regime A* close to the sample surface the electron cloud is confined in space and time, the electron density is high and *e–e* scattering events happen. In the *radially uniform force regime B*, the electron clouds expand isotropically in the shape of hemispherical shells. In the *non-uniform force regime C* beyond the anode the distributions flatten and slow and fast electrons approach each other again. The focus voltages are different in (a)–(d), note the different scale bar and anode voltage in (d).

shift extends to about 1 ns for the x-ray cases (c, d) and even several ns for the VUV/EUV cases (a, b), due to the small velocity difference. Although the separation proceeds much faster in (c, d), the x-ray cases are more critical than the low-energy cases due to the much larger amount of slow electrons. The larger velocity differences in panels (c, d) should show up in a broader Lorentzian as compared to the VUV/EUV range. Concluding, in regime *C* the Coulomb repulsion by the cloud of slow electrons is stronger for photoelectrons travelling close to the optical axis, leading to an *additional non-isotropic acceleration* of the photoelectrons with a maximum in the center of the distribution.

In order to estimate the number of electrons per pulse we consider some quantitative facts. The lowest photon intensity that we could use experimentally (due to the minimum possible slit width of 10 μm) was $\sim 10^5$ photons per pulse. The average escape depth of secondary electrons from a metal surface is 2.5 nm [31], for the fast photoelectrons the value is even lower. For $h\nu = 1000$ eV a few percent of the incoming beam, for 10 μm slit width $\sim 10^3$ photons, are absorbed in this region [32]. All absorbed photons will create photoelectrons distributed over the valence range and the (open) core-level and Auger channels, weighted by the ratio of the cross sections. Due to the rather small inelastic mean free path (IMFP) only a fraction of these electrons reaches the surface (at 60° off-normal the path length is already increased by a factor of 2). Most of the fast photoelectrons will be lost due to inelastic scattering processes, giving rise to a large number of cascade electrons. Assuming energy conservation, one primary electron (1000 eV) can give rise to about 200 secondary electrons

with energies equally distributed in the interval between E_F and 10 eV above E_F (corresponding to ~5 eV kinetic energy in vacuum). Due to the energy-dependence of the hot-electron lifetime the cascade has its intensity maximum right above the Fermi energy. However, only the high-energy fraction above the work function threshold can escape from the surface. The potential barrier of the surface not only acts as high-pass filter, but also induces a strong restriction in momentum space. Slow electrons leaving the surface experience strong refraction due to the inner potential $V_0 \sim 15$ eV for Ir. The 1 eV electrons filling the full half space on the vacuum side correspond to an 'escape cone' of only $+/-14°$ inside of the crystal. Hence, only electrons travelling close to the surface normal within a solid-angle fraction of 1.6% of 4π can escape from the surface.

At very low photon intensities, the stochastic nature of the emission process becomes relevant. There is never more than 1 escaping fast valence photoelectron per photon pulse and the probability that it is accompanied by a low-energy charge cloud tends to zero for very low intensities. In this limit the space-charge interaction vanishes. With increasing photon intensity more and more photoelectrons are created in a single pulse and most of them are scattered, causing the multiplication effect. From comparison with our simulation, we calculate sample currents of ~1 μA at the highest photon intensity of $\sim 10^7$ photons per pulse, corresponding to $\sim 10^6$ electrons per pulse at 5 MHz. Regarding the given photon flux (see experimental section), we estimate a total yield (photoelectrons and secondaries) of ~0.1.

Concluding these considerations, we point out that the expansion of the electron distributions with different energies shows a counter-intuitive behaviour. The distance between them does not continuously increase (as one might expect due to their initial relative velocities) but is a non-monotonous function of time. In the decelerating region, the faster electrons have been retarded more strongly at a given instant and hence the distance between populations shrinks in region *C* (figure 3(a)–(d)). We will discuss this phenomenon further in the framework of the theoretical model and see that the shape of the measured energy isosurfaces allows disentangling the isotropic and non-isotropic shifts and quantifying the amount of charge per pulse.

In pump-and-probe experiments the delay between pump pulse (creating low-energy electrons) and probe pulse (defining time zero for the photoelectrons) must be taken into account. For delays in the range of a few ps or less (as used for the study of ultrafast processes), the delay does not show up in the plots in figure 3. We expect that the space-charge shift does not change as long as the emission pattern of the laser-induced slow electrons is homogeneous and the total number of low-energy electrons does not change. For larger delays (>100 ps) Plötzing *et al* [8] have observed substantial changes in energy positions of the photoelectrons. This can be understood by shifting the time markers on the black trajectories in figure 3 to earlier times (i.e. to the right-hand side), leading to a deceleration of the photoelectrons. Since the electron cloud emitted by the pump pulse appears earlier, all photoelectrons have to cross the cloud and the *e–e* scattering probability might thus be significantly enhanced.

So far, all considerations are valid for metallic samples where excess charges are efficiently screened, yielding a constant, well-defined surface potential. The situation is different for semiconductors due to the surface photovoltage [33]. Optically-induced electron-hole pairs lead to a diffusion of carriers into the surface depletion zone. The transient change of carrier concentration reduces the band bending at the surface and generates an electric field when the pump pulse arrives, persisting until the carriers recombine (mostly radiatively). Yang *et al* [34] have observed that the outgoing photoelectrons are influenced by this short electric field pulse. Although the decay constant of the photovoltage is only 1.5 ps in the case of GaAs, the outgoing photoelectron experiences the transient field pulse for macroscopic delay times up to several 100 ps where the force exerted by the photovoltage pulse is still significant. The time scale depends on the photoelectron velocity. Note that this effect originates in a different surface potential, not in vacuum space-charge. In our experiment it would thus lead to a rigid displacement of the whole spectral distribution. Photovoltage-induced energy shifts are expected for a variety of semiconductors, topological insulators, or layered materials with reduced interlayer conductivity.

Figure 3 reveals one obvious advantage of the cathode-lens geometry for long pulses. By the time the late electrons of a 50 ps pulse (typical for synchrotron radiation sources) are emitted, the early ones have already travelled 1.5 mm away from the sample, thanks to the strong acceleration field. This strongly diminishes the electron density in the stochastic regime. With decreasing pulse length, however, this advantage is reduced.

3.2. Semi-analytical theory

In our analytical approach, we consider the slow secondary electrons to be a point charge, while the fast primary electrons form a shell. This approximation is particularly good for high energy photoelectrons, cf. figure 3. We can consider fast electrons to start at the same point, with velocities $\boldsymbol{v}_0 = (v_0 \sin\theta,\ v_0 \cos\theta) = (v_r,\ v_z)$, where θ is measured from the optical axis z, and we only consider one radial direction r. In the rest frame of slow electrons, which is at constant acceleration while in the uniform accelerating field, the shell of primary electrons expands isotropically.

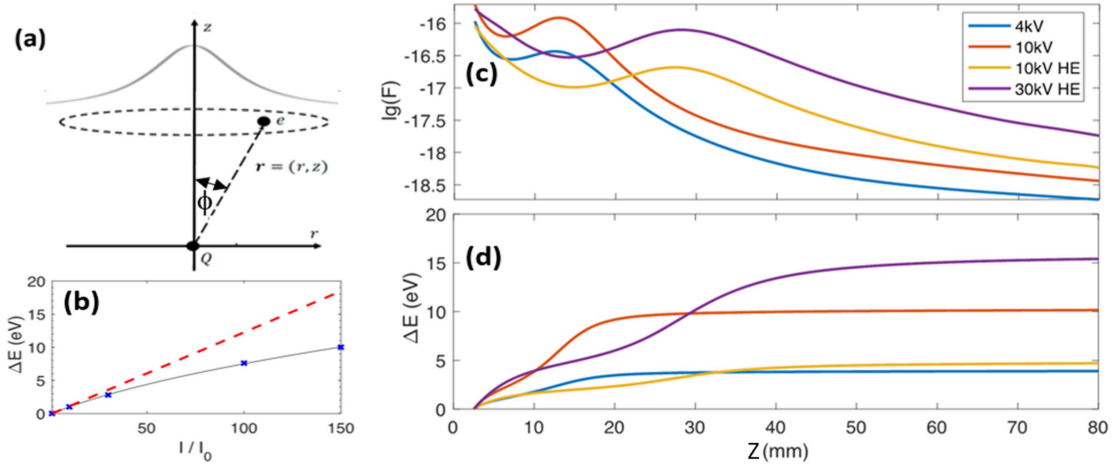

Figure 4. (a) Origin of the Lorentzian-shaped space-charge acceleration of the fast primary electrons (dashed momentum disc) by the slow secondary electrons modelled as a point charge Q; z is referred to the centre of gravity of the slow electron cloud. (b) Measured energy gain ΔE on the z-axis as function of photon intensity (dots) in comparison with the extrapolated initial slope (dashed line). (c) Calculated on-axis Coulomb force (on a log scale, −18 denotes attoN) and (d) space-charge induced energy gain for a 1 keV photoelectron and $Q = 1.3 \times 10^6$ e; here Z is referred to the sample surface. The four colours correspond to different anode potentials and two cathode-lens geometries (HE denotes the high-energy lens with 10 mm gap between sample and anode); details of the calculation see text.

For electric field strength ε, acceleration along z is given by $\mathrm{d}v_z/\mathrm{d}t = -e\varepsilon/m$ which is independent of $v_z(t = 0)$. As seen in regime *B* of figure 3, the spatial profile of the primary electrons remains spherical, see 100 ps distributions. As the first (on-axis) primary electrons exit the accelerating field, the rest of the spherical shell is still being accelerating along z. Upon exit of the accelerating field (at the centre of the anode bore in figure 3), the relative velocity in the axial direction between electrons at different starting angles is smaller than that in the radial direction. Equating the energy before and after acceleration under the assumption of a uniform field with a sharp cut-off at $z = L$, we can write

$$E_{\mathrm{kin}} = \frac{1}{2}m(v_0\cos\theta + \Delta v_z)^2 + \frac{1}{2}m\,v_0^2\sin^2\theta = \frac{1}{2}m\,v_0^2 + \mathcal{E}L. \tag{1}$$

Because of the concavity of the square-root function, this term is smaller for large $\cos\theta$, and hence small θ, that is for starting angles close to the axis. Electrons with larger initial axial velocity are accelerated less, so the velocity profile in region *C*, after passing through the acceleration field is *flattened* along the axial direction. This leads to the spatial profiles in figure 3, 200–400 ps distributions. For $\mathcal{E}L \gg mv_0^2$, the final axial velocity of the primary electrons is effectively uniform.

Once the spatial profile has flattened as in regime *C*, the effective situation is approximately that of a point charge Q of secondary electrons (black rays close to the axis in figure 3) repelling primary electrons in a radial disk. A sketch of this model is shown in figure 4(a), with the dashed circle denoting the disc of photoelectrons.

The axial force component is

$$F_z = F_{\mathrm{Coulomb}}\cos\phi = \frac{Qe}{4\pi\epsilon_0}\frac{1}{(r^2+z^2)}\frac{z}{\sqrt{r^2+z^2}} \propto \frac{1}{(r^2+z^2)^{3/2}} \propto \frac{1}{(1+\tan^2\phi)^{\frac{3}{2}}}. \tag{2}$$

To recover the real-space profile at the end of the trajectory, we would integrate twice

$$\Delta z(r) = \int_0^T\left(\int_0^{t''}\frac{F_z}{m}\mathrm{d}t'\right)\mathrm{d}t'' \tag{3}$$

for total ToF T. If, for a given electron, ϕ is independent of time, we can take all radial dependence out of the integral to get an integral of the form

$$\Delta z(r) = \frac{1}{(1+\tan^2\phi)^{3/2}}\int_0^T\left(\int_0^{t''} g(z(t'))\,\mathrm{d}t'\right)\mathrm{d}t'', \tag{4}$$

where g is not easily integrable, but crucially has no radial dependence.

As the observed relative shift in z between on- and off-axis electrons is small relative to the distance between primary and secondary electrons, we would expect this Lorentzian profile to be reflected in velocity, energy (square-root), and hence final position and ToF profiles. The measured energy gain ΔE (dots) on the axis as a

function of photon intensity is shown in figure 4(b). With increasing intensity, the slope of the curve is reduced in comparison with its initial slope (dashed line). The increasing amount of charge in front of the surface may act as a high-pass filter for slow electrons. The extrapolation shown in figure 4(b) reveals that even the distribution measured at the lowest photon intensity I_0 (10 μm exit slit) already shows a small space-charge acceleration of 250 meV. It means that at this comparatively low photon flux of 10^5 photons per pulse we are not yet in the regime where the photoelectron is not accompanied by secondary electrons (see discussion in section 3.1). The persistence of a space-charge induced shift in cathode-lens type instruments down to such low photon intensities underlines the importance of the correction shown below.

In fact, the inner shell of secondary electrons does also expand, strongly dependent on the focusing conditions of the lens, compare figure 3(a)–(d). Furthermore, we have neglected the acceleration in the radial direction, which varies throughout the disk. Significant radial forces would change the momentum distribution; however, this is not observed in the experiment. The double integral along the full trajectory is intractable, but the term in equation (4) is the dominant one in the deterministic part of the space-charge effect, and the profile of the shift seen in real data (figures 1, 2) is well-described by a Lorentzian. This assumption is validated by the quality of fit of a generic Lorentzian to the observed shift pattern (cf. figure 1(e)).

At realistic experimental conditions, the number of primary electrons is small and the Coulomb interaction within the shell of primary electrons can be neglected. In the experiments shown below, no more than one primary electron is recorded per photon pulse. This condition may change in future experiments at FEL sources where the number of photon pulses per second is much smaller (e.g. 27 000 for the European XFEL compared to typically 10^6 at storage rings) and the average photon intensity is similar. In pump-and-probe experiments the slow laser-induced electrons may alter the behaviour because the different instants of emission of slow and fast electrons lead to a shift in the centres of the expanding shells. The profile of the deterministic component would likely still be approximately Lorentzian, while the stochastic component may be increased for equal charge densities.

Forces on electrons travelling along the optical axis (shown logarithmically as a function of position in figure 4(c)) have been computed with distances extracted from SIMION using equation (2) and numerically integrated by adaptive quadrature [35] to give the energy gain ΔE of the on-axis fast electrons due to the repulsion by the secondary charge cloud (figure 4(d)).

Since the integral over the Coulomb force would diverge for $z \rightarrow 0$, we have to introduce an effective cut-off z_0 which accounts for an average initial distance of the interacting electrons. The value of z_0 can be determined experimentally. By fitting a Lorentzian profile to the observed isosurface at the Fermi energy (see figures in the experimental section), we can decompose the observed on-axis shifts into the isotropic part (asymptotic limit, offset of the Lorentzian) and non-isotropic part (amplitude of the Lorentzian). The effective z-cutoff and charge Q are derived from the fit by assuming a sharp transition between regimes B and C at the anode bore, requiring that the isotropic and Lorentzian components match those observed. For the maximum photon intensity studied, we calculate a charge of $Q = 1.3 \times 10^6$ e and a cutoff of $z_0 = 2$ mm. In calculating on-axis shifts for different geometries and anode potentials, we have assumed a constant effective early cutoff, which is to be validated in future experiments. It roughly corresponds to the initial spread of the electron distribution due to the pulse width of ~70 ps.

As a point of comparison, Long *et al* estimate the space-charge induced energy spread for a system with negligible pulse width (equation A1 in [6]). Plugging in our source-spot radius and maximal observed space-charge shift, we get an estimated secondary charge of approximately 10^5 e. Qualitatively, then, the calculated secondary charge from our simulation is reasonable, as the non-negligible pulse duration results in a larger average initial separation and thus a smaller effect.

The four curves in figure 4(c), (d) have been calculated for a cathode lens with 4 mm gap between sample and anode for two anode potentials (labelled 4 kV and 10 kV) and for a high-energy cathode lens with 10 mm gap and higher anode potentials (labelled 10 kV HE and 30 kV HE). Forces and resulting energy gain depend strongly on anode potential and lens geometry. For 10 kV anode voltage the energy shift is smaller by a factor of 2 for the larger lens (compare 10 kV and 10 kV HE). For both lens geometries, the shift increases with increasing anode voltage (cf. 4 kV and 10 kV as well as 10 kV HE and 30 kV HE). In the region of decelerating lens field (region *C* in figure 3) the fast and slow electrons approach each other again. The minimum distance decreases with increasing anode voltage and with decreasing geometric size of the lens. Minimisation of the space-charge shift thus demands a larger lens geometry and smaller anode voltages. However, the latter is connected with a sacrifice in *k*-resolution [19].

Concluding this section, we mention that the effect of re-approaching of fast and slow electrons was overlooked in the earlier work [11]. The Lorentzian is clearly visible in the space-charge simulation using the GPT code (cf. figure 6 of [11]). In view of the long-range Coulomb forces evident in figure 4(c), (d), it seems favourable to cut off the secondary electrons, exploiting the high-pass filter action of the high-energy objective lens by suitable lens settings as depicted in figure 5(a) of [11].

3.3. Correction algorithm

Rather than trying to predict the space-charge induced energy shifts quantitatively, we take a hybrid approach, whereby we assume the following generic functional form of the space-charge effect, which is then fitted to the observed data

$$t_{\mathrm{F}}(x,\,y) = t_{\mathrm{F}}^{0} - \frac{a\,b^{3}}{(b^{2} + (x - x_{0})^{2} + (y - y_{0})^{2})^{3/2}} \tag{5}$$

$$\Delta t_{\mathrm{F}}(x,\,y) \propto \frac{Q}{(b^{2} + (x - x_{0})^{2} + (y - y_{0})^{2})^{3/2}}. \tag{6}$$

Here, x, y refers to the spatial coordinates along the screen, while successive slices are labelled by their ToF t. A given profile in axial position z in the moments before impact translates directly to the same temporal profile in the recorded time-slices.

The shape of the space-charge effect is clearly visible at the Fermi energy (figure 1(e)), so the quantity $t_{\mathrm{F}}(x,\,y)$ we are investigating is the ToF corresponding to the Fermi edge, which varies across the screen. The free parameters are the centre of the Lorentzian $(x_0,\,y_0)$; the base Fermi ToF t_F^0, which corresponds to the ToF for electrons with uniform space-charge interaction; the magnitude of the effect a, which gives the maximal difference in ToF between starting angles 0 and π; and the parameter b, which controls the radial width of the Lorentzian. As the model exhibits radial symmetry, we consider a circular profile with width b, rather than a more generic elliptical profile.

For a given pixel on the detector (spatially-resolving delay-line detector), the ToF corresponding to the Fermi edge is determined by a threshold between when the count is zero (within noise) and non-zero. This is sampled for a range of $(x,\,y)$ positions, and the five parameters $(x_0,\,y_0,\,t_{\mathrm{F}}^0,\,a,\,b)$ are fit to the samples by means of the Levenberg–Marquardt algorithm [36] for unconstrained optimisation. Having obtained these parameters from the fit, the complete $t\,(x,\,y)$ data stack is corrected by adjustment of the ToF values using the Lorentzian functional as 'zero' reference, yielding a planar Fermi surface t_F^0 and hence a planar Fermi momentum disc $(E_{\mathrm{B}} = 0, k_x, k_y)$.

Time-slices correspond to layers of voxels with a specific ToF, while the above procedure generates a continuously valued function, so we linearly interpolate between voxels, which preserves the total count.

Since the force is proportional to the macrocharge Q (see equation (2)), Q appears as scaling factor in front of the integrals in equations (3) and (4) and also in the functional form equation (6). This scaling with Q opens the possibility of correcting even distributions with strongly fluctuating pulse-to-pulse intensities, a prominent example being SASE-type FELs. In the data streaming architecture each photon pulse is monitored concerning time and individual pulse energy. Assuming that Q is approximately proportional to the intensity of a given photon pulse, each counting event can be corrected according to equation (6) by its individual correction factor, depending on Q. The gross effect of space-charge shifts for strongly fluctuating intensities can thus be eliminated.

Having access to the full spectral distribution functions $I\,(E_{\mathrm{B}}, \boldsymbol{k})$ in a momentum range exceeding the first Brillouin zone and several eV range of binding energy, we can apply further data treatment and corrections. The following routines have been implemented into an automated processing pipeline (see appendix): Time-to-energy conversion, correction of chromatic aberration, tilt of the optical axis and image-field curvature, as well as elimination of (periodic) detector artefacts by Fourier-filtering in logarithmic space. In practice, most or sometimes even all of these contributions are negligible. The significance of the different terms depends on the experimental conditions and the settings of the electron optics. Space-charge shifts are corrected routinely, even if they are in the 100 meV range. Uncorrected data stacks would lead to missing parts of the Fermi surface, even for such small shifts.

3.4. First practical result of space-charge correction algorithm in Fermi-surface imaging

Figure 5 shows how the space-charge correction acts on a 4D data stack as needed for mapping of the Fermi surface and Fermi velocity, here for the prototypical high-Z material W(110). The top row shows the as-measured momentum distributions at the Fermi energy for three different photon energies, corresponding to three different values of k_z as marked in (g). Direct transitions into a free-electron like final state band, with the photon energy determining the momentum perpendicular to the sample surface allow to measure size, shape and topology of the 3D Fermi surface. Technically, data arrays taken at sufficiently many photon energies are concatenated, in a tomographic-like manner (for details, see [20, 37]). Panels (d–f) show the Fermi-energy cuts of the same data arrays after space-charge correction. The centres of the images look practically identical, however with increasing distance from the centre, band features change size or become more intense (cf. arrows in (d, e)) or additional features appear (arrows in (f)). In the experimental Fermi surface, these subtle differences

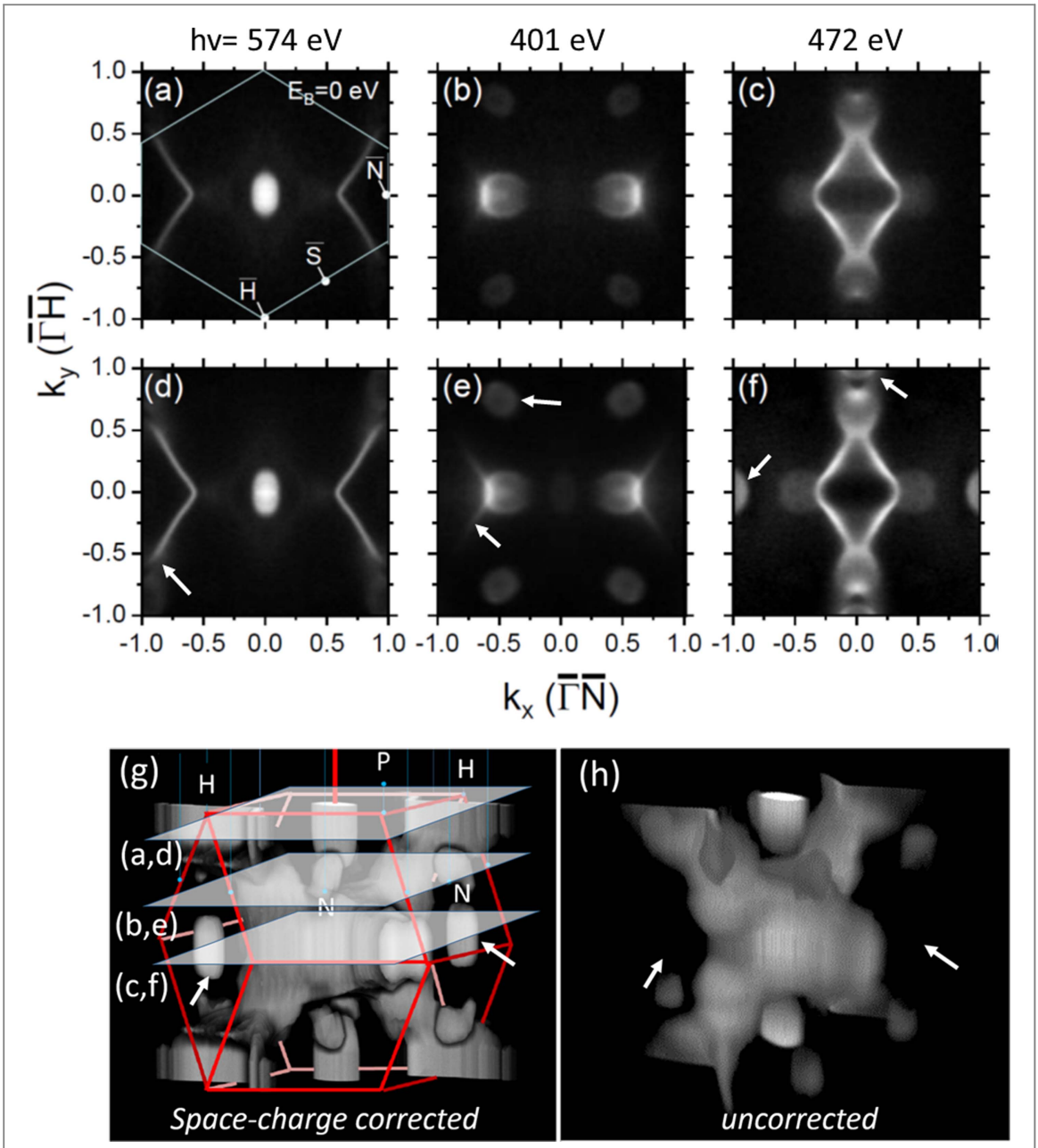

Figure 5. Energy isosurfaces for photoemission from W(110) before (a)–(c) and after space-charge correction (d)–(f), taken at the photon energies stated on the top. The white lines in (a) mark the surface Brillouin zone; $\overline{N}$, $\overline{H}$ and $\overline{S}$ denote high-symmetry points. Before correction the outer regions of the *k*-patterns are weak or even missing (see arrows in (d)–(f)). In the Fermi surface derived from corrected (g) and uncorrected sections (h) the missing features lead to deformations or missing outer hole pockets (see arrows).

lead to the disappearance of some of the ellipsoid-shaped hole pockets (arrows in (g and h)). This is most clearly seen in the 'k-space movies' in the supplementary material.

The results for tungsten shown here and in the supplementary material have been taken with standard settings as used in [20, 37], with rather small space-charge shifts of <1 eV. Nevertheless, the subtle differences between uncorrected (a–c) and corrected Fermi-energy cuts (d–f) show up strikingly in terms of missing parts in the experimental Fermi surface.

Given the present state of knowledge it is not possible to directly compare these results with previous work using dispersive spectrometers [1–9]. In a cathode lens we have the special behaviour of trajectories of fast and slow electrons as sketched in figure 3, whereas in conventional spectroscopy the electrons travel for typically 60 mm in the field-free region in front of the sample. Electrons with kinetic energies of 1000, 120 and 16 eV pass this distance in 3, 9 and 24 ns, respectively; a time scale much longer than that of figure 3. The simple model of a spherical electron cloud in the field of a point-symmetric capacitor [6] predicts the same magnitude of space-charge shift and broadening as a true multi-particle simulation [7]. In the latter theoretical paper and experimental data using a HHG source [8] shift and broadening have approximately the same value. In recent

work at the FEL source SACLA, SPring-8, Japan [5, 29] the measured broadening was found to be larger than the measured shift (by up to one order of magnitude) as well as larger than the simulated shift. From figure 1(e) we conclude that in our raw data the width of the Fermi cutoff is at least one order of magnitude smaller than the energy shift on-axis (at sufficient angular resolution). After correction, the energy width is two orders of magnitude smaller than the initial energy shift (figure 2(f)–(i)). A quantitative estimation of the space-charge limit for dispersive spectrometers in comparison with that of cathode-lens instruments would require comparative measurements at similar conditions; this was not intended in the present work. In particular, the positive sample bias for rapid redirecting of the secondaries as mentioned in [7] and our high-pass cutoff in the objective lens have both not been explored yet.

4. Conclusion

The spatio-temporal confinement of the electrons released by intense, short photon pulses in a small area on a solid sample leads to significant Coulomb interaction, which alters the energy and angular distribution and sets the ultimate limit to the performance of photoemission experiments. In the present work we have explored the space-charge effect by means of experiments in the soft x-ray range, revealing large space-charge induced energy shifts of up to 10 eV at the conditions of the high-brilliance soft x-ray beamline P04 at the storage ring PETRA III at DESY, Hamburg. In working towards a solution of this problem we developed a semi-analytical theory, supported by ray-tracing simulations. In particular we studied the case of momentum microscopy, providing complete $I(E_{\mathrm{kin}}, \boldsymbol{k})$ data sets that reveal the space-charge induced shifts in a single measurement for an energy range comprising the *d*-band complex of a transition metal and a momentum range exceeding the Brillouin zone. The aim of the investigation was to test a new way of space-charge correction and elucidate the limit of experimental conditions that still yield usable photoemission data.

Starting from the analytical model, a correction algorithm was developed that eliminates the deterministic part of the Coulomb interaction. This contribution results from the net force exerted on a given photoelectron by all other electrons. Calculations and experiments reveal that the deterministic contribution arises in the form of a Lorentzian-shaped deformation of the photoelectron energy isosurfaces. The main effect is an acceleration of the photoelectrons due to Coulomb repulsion of the large amount of slow secondary electrons. This acceleration is anisotropic because the secondary electron cloud travels slower and expands less than the photoelectron cloud. The correction is based on the experimentally-measured deformation of the electron distributions at the Fermi-level cutoff. A generic functional form of the space-charge induced energy shift is fitted to the observed Fermi isosurface. This fit yields the required parameters for the subsequent correction of the complete data array. In addition, the fit gives the value of the charge of slow electrons that cause the main part of the energy shift. What remains after the correction is the contribution of individual *e*–*e* scattering processes reflecting the stochastic nature of the photoelectron beam. The stochastic contributions cause an irreversible blur of the band features and a strongly enhanced inelastic background. This non-deterministic mechanism, sometimes referred to as 'stochastic heating' of the beam [38], defines the ultimate limit of the tolerable intensity of pulsed photoemission experiments.

In the characteristics of the interaction we can distinguish three regimes: initially, the electron density is very high and the interaction is dominated by stochastic scattering processes. The photoelectrons of a given energy then expand as a hemispherical shell, and hence separate from the cloud of slow secondary electrons. In this phase the net Coulomb force is radially uniform. In the decelerating lens field beyond the anode, the photoelectron shell flattens, and hence the force becomes non-uniform. Its maximum occurs in the centre of the photoelectron distribution, thus causing the Lorentzian deformation. The net action of this non-uniform force depends crucially on the lens geometry and the voltage of the anode. For larger lens geometries and smaller anode potentials the shifts are substantially reduced. This non-uniform force regime has been overlooked in earlier work [11], although the Lorentzian was clearly visible in the space-charge simulation using the GPT code (cf. figure 6 of [11]).

The experimental results confirm the predictions of the theoretical model for the deterministic contribution. The measured distributions further reveal important details of the stochastic contribution: In an energy interval of about 1 eV below the Fermi edge the bandstructure persists up to high intensities (figure 2(h), (i)). This proves that the majority of photoelectron scattering events involves a slow electron so that the photoelectron loses energy. The inelastically-scattered electrons appear as strongly enhanced diffuse background in the region several eV below E_F. Hence the electrons observed close to the Fermi cutoff did not suffer from loss scattering, which means that high space-charge shifts can be tolerated especially for Fermi-surface imaging or bandmapping close to E_F. At high intensities a visible size reduction of the bandstructure patterns appears, giving evidence of a loss of (transversal) momentum of the photoelectrons. Such 'fast *e*—slow *e*' scattering events can only occur before the energetic separation, i.e. very close to the sample surface (*stochastic*

regime A in figure 3). High-pass filtering in a special geometry of the objective lens allows to remove the slow electrons in the lens field.

Due to the rather narrow spin-asymmetry profiles, the results of the present study have essential consequences for spin-filtered *k*-imaging in the presence of significant space-charge shifts. The space-charge induced energy shifts must be accounted for in the setting of the spin filter in order to retain the optimal working point of the spin filter.

The theoretical and experimental results of the present work provide valuable design criteria for the development of next-generation *k*-space microscopes with minimised sensitivity to Coulomb interaction in the beam. An inherent problem of SASE-type free electron lasers is their strongly fluctuating pulse-to-pulse intensity. In the data-recording routine each individual counting event is labelled with the time and intensity parameters of the corresponding photon pulse. Given the information on pulse intensity, the analytical expression for the correction will allow removal of the main part of the energy shift even in such cases of strong (but known) intensity fluctuations. First pump-and-probe experiments with fs sources leave no doubt that the space-charge problem is the central obstacle of future photoemission work at pulsed high-brilliance photon sources. The present study raises some hope that we are not defenceless to these effects.

Acknowledgements

We thank the staff of PETRA (beamline P04) for excellent support during the measurements. Sincere thanks go to Christian Tusche, Forschungszentrum Jülich, for fruitful cooperation and discussions and to Kai Rossnagel, Universität Kiel for a critical reading and constructive comments. The project was funded by BMBF (05K13UM2, 05K13GU3, 05K16UM1) and DFG (Transregio SFB/TRR 173 'Spin+X').

Appendix A. Formalising operations on the measured arrays

The 4D spectral density $\rho(E;\ k_x,\ k_y,\ k_z)$ fully describes the properties of the band structure of interest. In particular, let us denote by supp(ρ) the *support* of the density, which is defined as the set of points in the space defined by (E, $\boldsymbol{k}$) for which ρ is non-zero. In other words, at $T = 0$, it gives the set of points defining occupied bands. In particular, we restrict ρ to the (3D) subspace at the Fermi energy $E = E_F$, and further introduce the set-theoretic operator ∂ to denote the *boundary* of a set. Formally, the boundary ∂S of a set S refers to the set of points with a neighbourhood including at least one point in both S and the complement of S. Intuitively, in our Euclidean space, it refers to the surface that bounds one or several volumes. This notation may be familiar from Stokes' theorem in vector calculus, and corresponds to the intuitive notation that for a sphere $\mathrm{d}V = \mathrm{d}\frac{4}{3}\pi r^3 = 4\pi \mathrm{r}^2\mathrm{d}r = A\mathrm{d}r$, for a spherical shell of surface area A.

Using this notation, we can define the Fermi surface, which separates occupied from unoccupied states at the Fermi energy, as

$$S_F = \partial\ \mathrm{supp}(\rho(k_x,\ k_y,\ k_z,\ E = E_F)).$$

Note that in general, the support may be discontinuous, which leads to a fragmented Fermi surface.

In order to properly describe the corrections described in the paper and the supplement, we need to be more specific about what is being measured in our photoemission experiments, that is by addressing the correspondence between the experimentally measured array I and the underlying spectral density ρ. The photoemission process yields a representation of ρ that is weighted by the matrix element (and possibly by symmetry selection rules when polarised radiation is used [39]). The delay-line detector (DLD) consists of a 2D array of (virtual) pixels that record discrete counts of incoming electrons in an exposure time Δt. The recorded data come in the form of an array of these counts, with the intervals of discretization set by the DLD software (for details, see [40]). For a given run, k_z is defined in k-space by the intersection of a spherical shell (whose diameter is defined by the photon energy and its centre is displaced by the vector of the photon momentum which completely ends up in the electron momentum [39]) with the periodic pattern of Brillouin zones, while k_x and k_y index position along the screen.

We can consider the spectral density to be a 'count' density. Then, pixel intensities are given by integrals over the 3D voxels given by the spatial extent of the pixel and exposure time, centred on ($\mathrm{k_x}$, $\mathrm{k_y}$, t(E))—for a fixed k_z

$$I(q_x,\ q_y,\ q_z,\ E) \propto \int \mathrm{d}k_x \mathrm{d}k_y \mathrm{d}t\ \rho(k_x,\ k_y,\ k_z = q_z,\ t(E)).$$

To infer ρ from I, we need to know about the relationship between time and electron energy (cf. B), the relationship between coordinates on the screen and the wavevector (cf. C–E), and dependencies of intensity with position independent of ρ (cf. F).

Affine mappings between coordinate systems are given by (affine) transformation matrices, giving transformations $\boldsymbol{q} \rightarrow \boldsymbol{q}'$ of the form $\boldsymbol{q}' = M\boldsymbol{q}$, where to allow translations, we use projective coordinates (q_x, q_y, 1). To apply these transformations to images, we take the midpoint of a pixel in the new coordinate system, apply the inverse transform M^{-1} to identify the corresponding location in the old coordinate system, and calculate the new pixel value by (bilinear) interpolation between the four closest corresponding old pixels.

Appendix B. Time to energy conversion

Individual images acquired by the delay-line detector are equally spaced in time. However, to obtain the electronic band structure to investigate physical properties, the quantity we wish to measure is $\rho(E; \boldsymbol{k})$, which requires converting from the time scale to energy. For a constant velocity, we would have

$$v \propto \sqrt{E} \quad \text{and} \quad t \propto \frac{1}{v} \propto \frac{1}{\sqrt{E}}.$$

In practice these relations are only approximate because the velocity varies along the ray path. To obtain the functional relationship for the present system, we use finite element simulation [27] yielding specific (t, E) pairs for a range of values spanning those observed experimentally, and use them to approximate the mapping by polynomial interpolation.

This approximation is non-linear, so at higher energies, the constant difference in energies corresponds to a smaller ToF difference than at lower energies. To account for this, we calculate the effective time difference between slices, as a ratio of the original time spacing, and scale all intensities by this ratio. By doing this, intensities correspond to counts in a specific energy window of fixed width.

Appendix C. Chromatic aberration of magnification

As a result of chromatic aberration, slices at different energies can be subject to varying degrees of magnification [13]. To find the energy dependence of this magnification, we computed magnification values at 10 energies in the observed range by finite element simulation [27] and, linearising in the observed range, determine the linear functional relationship between energy and magnification by ordinary least squares. After converting from the time scale to energy, we correct the aberration by calculating the affine transformation matrix corresponding to the rescaling by a factor of $s = s(E)$ [41]

$$M_{\text{scale}} = \begin{pmatrix} \text{s} & 0 & 0 \\ 0 & \text{s} & 0 \\ 0 & 0 & 1 \end{pmatrix}.$$

To recover the physical relevant quantity of counts per voxel, we rescale intensities to maintain the total number of counts per slice. A square of initial area 1 has area s^2 after transformation, so we rescale intensities by this value to retain the total count.

Appendix D. Field curvature

As in every electron microscope the electron optics may also introduce barrel and pincushion distortions as a result of image-field curvature [13]. To correct these, we approximate the distortion by a shear transformation, which is valid for small imaged regions. The shear angle α is determined by requiring the appropriate reflection symmetries, and the following affine transformation is applied to all images in a stack

$$M_{\text{shear}} = \begin{pmatrix} 1 & \text{a} & 0 \\ 0 & 1 & 0 \\ 0 & 0 & 1 \end{pmatrix},$$

where $a = \cot\alpha$. Since the transformation is affine and does not involve a scale factor, total intensities are preserved.

More generally, radial distortion can be modelled by the transformation

$$r \rightarrow r(1 + k^* r^2)$$

for distortion parameter k. To apply this to images, we transform to radial coordinates centred on the symmetry point of the distortion, and calculate intensities by interpolation, scaling intensities by a factor of $\frac{1}{1+3kr^2}$, to conserve total counts.

Appendix E. Tilt of the optical axis

Magnetic stray fields of non-centric adjustment may result in an energy-dependent position of the beam centre in the image. To correct this tilt of the optical axis through a stack of images, the centre of symmetry is determined for slices early and late in the stack, and the relationship is linearised (in a region of a few eV) to obtain translation matrices for all slices in the stack of the following form:

$$M_{\mathrm{trans}} = \begin{pmatrix} 1 & 0 & \Delta x \\ 0 & 1 & \Delta y \\ 0 & 0 & 1 \end{pmatrix}$$

for translation $(x, y) \rightarrow (x + \Delta x, y + \Delta y)$. As all transformations retain the optical mask entirely within the image, this transformation retains the correct count density.

Appendix F. Detector artefacts

As a result of the periodic arrangement of the delay-line detector a systematic gridded artefact can be superimposed on the images (identical in each image). Specifically, the artefact appears to be multiplicative, of the form

$$I'(\boldsymbol{r}) \rightarrow I(\boldsymbol{r})(1 + a \sin \boldsymbol{b} \cdot \boldsymbol{r})$$

for magnitude a and grid direction $\boldsymbol{b}$.

To remove this artefact, we applied Fourier filtering in logarithmic space. Fourier theory assumes additive superposition of frequencies, so to apply it to the present case, we write the grid artefact in the form

$$\log I'(\boldsymbol{r}) \rightarrow \log I(\boldsymbol{r}) + \log(1 + a \sin \boldsymbol{b} \cdot \boldsymbol{r}).$$

In this representation, the two-dimensional discrete Fourier transform [42] reveals pronounced maxima corresponding to spatial frequency of the grid and its harmonics. Other periodic features of the slices are not as pronounced as these frequencies, which enables the use of MAXLIST, an algorithm for finding local maxima [43, 44] for identifying the frequencies that need to be suppressed. This is done by multiplying the image by a notch filter, which is 1 everywhere except for Gaussian 'notches' centred on each found peak. Converting back from frequency to real-space by taking the inverse Fourier transform reproduces the same images with the grid artefact removed. As the frequencies around 0 are not affected, the total intensity of the image is conserved.

Appendix G. Video comparison of tungsten Fermi surface

In the supplementary materials, we provide a video that compares the Fermi surface of tungsten as measured, with (left) and without (right) space-charge correction. As remarked for panels g–h of figure 5 in the main text, there are prominent features (e.g. some of the hole pockets at the N-points) missing in the uncorrected surface.

References

[1] Suga S and Sekiyama A 2014 *Photoelectron Spectroscopy* (Berlin: Springer)
[2] Dell'Angela M *et al* 2015 *Struct. Dyn.* **2** 025101
[3] Hellmann S, Hellmann S, Rossnagel K, Marczynski-Bühlow M and Kipp L 2009 *Phys. Rev.* B **79** 035402
[4] Hellmann S *et al* 2010 *Phys. Rev. Lett.* **105** 187401
[5] Oloff L-P *et al* 2014 *New J. Phys.* **16** 123045
[6] Long J P *et al* 1996 *J. Opt. Soc. Am.* B **13** 201
[7] Verna A, Greco G, Lollobrigida V, Offi F and Stefani G 2016 *J. Electron Spectrosc. Relat. Phenom.* **209** 14
[8] Plötzing M, Adam R, Weier C, Plucinski L, Eich S, Emmerich S, Rollinger M, Aeschlimann M, Mathias S and Schneider C M 2016 *Rev. Sci. Instrum.* **87** 043903
[9] Schiwietz G, Kühn D, Föhlisch A, Holldack K, Kachel T and Pontius N 2016 *J. Synchrotron Rad.* **23** 1158
[10] Oloff L-P *et al* 2016 *J. Appl. Phys.* **119** 225106
[11] Schönhense G, Medjanik K, Tusche C, de Loos M, van der Geer B, Scholz M, Hieke F, Gerken N, Kirschner J and Wurth W 2015 *Ultramicr.* **159** 499
[12] Boersch H 1954 *Zeitschr. Physik* **139** 115
[13] Hawkes P W and Kasper E 1996 *Principles of Electron Optics* (Amsterdam: Elsevier)
[14] Chao L C and Orloff J 1997 *J. Vac. Sci. Technol.* B **15** 2732
[15] http://scientaomicron.com/en/products/da30-arpes-system/
[16] http://specs.de/cms/front_content.php?idcat=366
[17] Ovsyannikov R *et al* 2013 *J. Electron Spectrosc. Relat. Phenom.* **191** 92
[18] Berntsen M H, Götber O and Tjernberg O 2011 *Rev. Sci. Instrum.* **82** 095113
[19] Tusche C, Krasyuk A and Kirschner J 2015 *Ultramicr.* **159** 520
[20] Medjanik K *et al* 2017 *Nat. Materials* **16** 615

[21] Schäfer E D, Borek S, Braun J, Minar J, Ebert H, Medjanik K, Kutnyakhov D, Schönhense G and Elmers H J 2017 *Phys. Rev.* B **95** 104423
[22] Kutnyakhov D *et al* 2016 *Sci. Rep.* **6** 29394
[23] Elmers H J *et al* 2016 *Phys. Rev.* B **94** 201403 (R)
[24] Oelsner A, Schmidt O, Schicketanz M, Klais M J, Schönhense G, Mergel V, Jagutzki O and Schmidt-Böcking H 2001 *Rev. Sci. Instrum.* **72** 3968
[25] Oelsner A, Rohmer M, Schneider C, Bayer D, Schönhense G and Aeschlimann M 2010 *J. Electron Spectrosc. Relat. Phenom.* **178** 317
[26] Viefhaus J, Scholz F, Deinert S, Glaser L, Ilchen M, Seltmann J, Walter P and Siewert F 2013 *Nucl. Instrum. Meth.* **710** 151
[27] Manura D and Dahl D 2008 SIMION (R) 8.0 User Manual (Scientific Instrument Services, Inc. Ringoes, NJ 08551, (http://simion.com/)
[28] Zhou X L *et al* 2005 *J. Electron Spectrosc. Relat. Phenom.* **142** 27
[29] Oloff L-P *et al* 2016 *Sci. Rep.* **6** 35087
[30] Bauer E 2012 *Ultramicr.* **119** 18
[31] Nakajima R, Stöhr J and Idzerda Y U 1999 *Phys. Rev.* B **59** 6421
[32] http://henke.lbl.gov/optical_constants/filter2.html
[33] Kronik L and Shapira Y 1999 *Surf. Sci. Rep.* **37** 1–206
[34] Yang S-L, Sobota J A, Kirchmann P S and Shen Z-X 2014 *Appl. Phys.* A **116** 85
[35] Shampine L F 2008 *J. Comput. Appl. Math.* **211** 131
[36] Levenberg K 1944 *Q. Appl. Math.* **2** 164
[37] Elmers H J, Kutnyakhov D, Chernov S V, Medjanik K, Fedchenko O, Zaporozhchenko-Zymakova A, Ellguth M, Tusche C, Viefhaus J and Schönhense G 2017 *J. Phys. Condens. Matter* **29** 255001
[38] Debernardi N, van Vliembergen R W L, Engelen W J, Hermans K H M, Reijnders M P, van der Geer S B, Mutsaers P H A, Luiten O J and Vredenbregt E J D 2012 *New J. Phys.* **14** 083011
[39] Schönhense G *et al* 2017 *Ultramicr.* **183** 19
[40] http://surface-concept.com/
[41] Hartley R and Zisserman A 2003 *Multiple View Geometry in Computer Vision* (Cambridge: Cambridge University Press)
[42] Jones E SciPy: Open Source Scientific Tools for Python, 2001-, (http://scipy.org/) (Accessed: 18 February 2017)
[43] van der Walt S, Schönberger J L, Nunez-Iglesias J, Boulogne F, Warner J D, Yager N, Gouillart E, Yu T and the scikit-image contributors 2014 scikit-image: image processing in Python *PeerJ* **2** e453
[44] Douglas S C 1996 *IEEE Trans. Signal Process.* **44** 2872